Materials Advances

ROYAL SOCIETY OF CHEMISTRY

PAPER

View Article Online
View Journal | View Issue

Cite this: *Mater. Adv.*, 2025, 6, 6919

Optical and photothermal properties of $CsWO_3$ nanoparticles endow poly(dimethylsiloxane) fluidic lenses with non-invasive thermo-optic and thermo-expansion effects for fluorescence imaging

Yu-Hang Cheng, Sheng-Yu Kao, Ming-Hsuan Ho, Jui-Wen Pan and Po-Sheng Hu *

The capabilities of $CsWO_3$ nanoparticles to transmit in the visible range from 400 nm to 650 nm and undergo strong near-infrared photothermal conversion from 750 nm to 2400 nm may make them functional materials in the fabrication of focus-tunable optical lenses. In this research, the noninvasive focal length tuning of a poly(dimethylsiloxane) (PDMS)-structured fluidic lens by near-infrared irradiated cesium tungsten oxide nanoparticles ($CsWO_3$ NPs), which generates heat and induces photothermal and thermo-optic effects on PDMS, was explored. The temperature-dependent mechanical property of PDMS and the stoichiometric, structural and photothermal properties of $CsWO_3$ NPs were characterized. Young's modulus ranged from 4.5 MPa to 3.7 MPa as the temperature of the PDMS sample increased from 25 °C to 48 °C and allowed a delicate tuning of the fluidic lens' front focal length from 21.02 mm to 20.89 mm when the near-infrared (NIR) optical power density increased from 0 mW cm^{-2} to 226 mW cm^{-2} while retaining the concentric shape of the focused beam spot. The fluidic lens was then incorporated into the detection arm of a light sheet fluorescence microscope, and it successfully captured the contrast-enhanced images of the fluorescein-coated $CsWO_3$ NPs.

Received 5th May 2025,
Accepted 8th August 2025

DOI: 10.1039/d5ma00435g

rsc.li/materials-advances

1. Introduction

The photothermal property of plasmonic nanoparticles (NPs) has increasingly drawn great attention for advances in many optics-related science and engineering fields. Upon photo irradiation, the plasmonic NPs are electronically excited causing a collective oscillation of electrons and subsequently relaxed by releasing heat energy.[1] This phenomenon opens up broad avenues for practical applications. For instance, by incorporating NPs of gold (Au), silver (Ag) and zirconium carbide coated with Au alongside a proper particulate size and concentration, the photo-absorbing capability of base fluids can be greatly enhanced, thus improving the efficiencies of solar energy collectors.[2,3] Additionally, Palermo *et al.* demonstrated the alignment of a nematic liquid crystal (LC) using light polarization-modulated heat generated by a photo-irradiated AuNP layer deposited on a thin dielectric layer of dimethylformamide-dissolved azo-dye.[4,5] Moreover, the integration of plasmonic AgNPs into wearable devices made of elastic polyurethane was found instrumental in promoting self-healing of the deformed composite film and removing fog on the device surface when illuminated with sunlight.[6] Likewise, ring resonators were constructed using a silica microsphere and a microcapillary through the embedding and infusion of an iron oxide NP solution, respectively, whose resonance wavelength can be photothermally shifted in the range from 3.3 nm up to 13 nm with a tunability efficiency of up to 2 nm mW^{-1}.[7,8] Other creative applications of heat generated by plasmonic NPs upon photo-irradiation were proven effective in the modulation of light amplitude by photothermally controlling the size of bubbles and in induction of changes in optical phases by two-wave mixing *via* embedding a single Au NP and Au–Pt NPs in a nematic liquid crystal film and a TiO_2 matrix, respectively.[9,10]

To date, although the photothermal effects of plasmonic NPs have shown potential in optical phase-modulation, light attenuation and selection of resonance wavelength, no research study on the fabrication of a focus-tunable optical lens using plasmonic NPs has been reported. One exception is an investigation study on a patterned Au nanorod array that creates a varying distribution of the optical refraction index for light focusing on NIR-irradiation; however, it requires some

College of Photonics, National Yang Ming Chiao Tung University, Tainan City, Taiwan. E-mail: pshu67@nycu.edu.tw

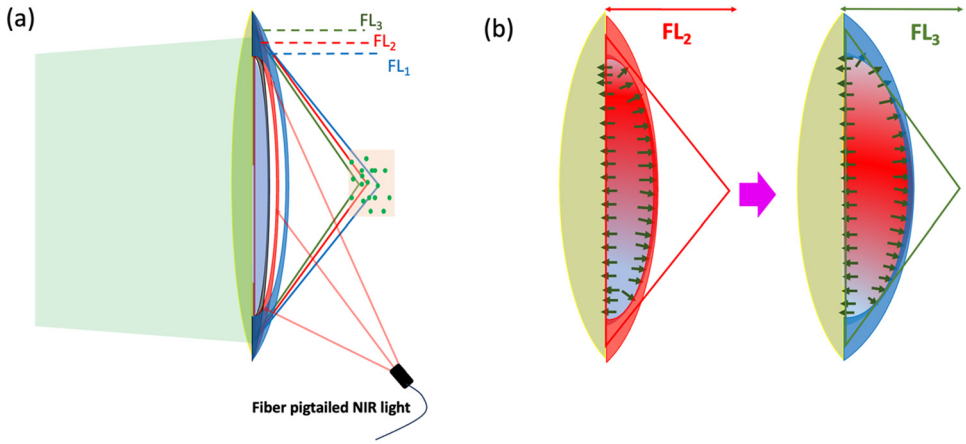

Fig. 1 Schematic of (a) the focusing property of the $CsWO_3$ NP solution-filled PDMS fluidic lens upon NIR irradiation and (b) the result of heat convection within the fluidic chamber that renders the transfer of heat through heat conduction from water medium to PDMS.

complicated fabrication processes and enables a tuning range of merely 16 μm.[11] Hence, this present study proposed an alternative mechanism which, on the basis of photothermal conversion of the plasmonic NPs that function as optical materials as well as heat generators *via* the side-illuminated NIR irradiation, modulates the thermo-optic and thermo-expansion effects of a poly-dimethylsiloxane (PDMS)-structured fluidic lens, as shown in Fig. 1(a), which has an empty fluidic chamber to be filled with the plasmonic NP solution. Thus, the main aim of this study is to explore and interrogate the feasibility of tuning the focal length of the fluidic lens *via* the optical and volumetric responsiveness of PDMS to the photothermal effect of plasmonic NPs by constructing an applicable lens and implementing it in a custom-made light sheet fluorescence microscope (LSFM), which necessitates optical components with transparency in the least range of visible wavelength from 400 nm to 650 nm, considering both sample excitation and signal collection. Fig. 1(b) depicts the direction of heat transfer from the water medium to the PDMS lens frame *via* thermal conduction as the incremental optical power density increases, which varies the focal length. Mechanistically, the thermal energy generated by the NIR-irradiated NPs initiates heat convection and results in a thermal distribution for a given input power density, thus varying the focal length through thermal conduction, accordingly. An increase in the input optical power density further increases the temperature of the NP solution as well as strengthens the thermal distribution, thus shortening the focal length of the PDMS lens.

Thus far, among all NP material systems capable of the photothermal effect when irradiated with the NIR light source, both AuNPs and Fe_3O_4 NPs have a size-dependent dominant absorption peak stretching from 450 nm to 550 nm with the feature size ranging from 12 nm to 41 nm and from 11 nm to 15 nm, respectively,[12,13] and iron platinum (FePt) NPs can absorb more than 70% of the entire visible (VIS) wavelength range,[14] which are not suitable for sample excitation at blue and yellow wavelengths. Furthermore, the gradually increasing optical absorbance of graphene oxide NPs toward 300 nm exhibits low NIR absorption, requiring at least 2 W cm^{-2} at 5 μg mL^{-1} to reach beyond 55 °C.[15] Likewise, although CuS NPs exhibit low absorption from 500 nm to 700 nm alongside an absorption peak at 960 nm, about 1 W cm^{-2} at 808 nm was required to reach 60 °C,[16] which may cause material breakdown when a low power threshold material is used for the structure of the fluidic lens.

Furthermore, not only are the $CsWO_3$ NPs highly transmissive in the VIS wavelength range from 450 nm to 750 nm, particularly suitable for sample excitation and fluorescence collection, but they also exhibit strong absorption in the wavelength range from 750 nm to 2400 nm, attaining 37 °C with a power density of 0.7 W cm^{-2} at 980 nm.[17] Such optical power may be sufficient to induce the thermo-optic and thermo-expansion effects of PDMS and drastically reduces the risk of material breakdown when illumination is prolonged. Therefore, the $CsWO_3$ NP solution is chosen as the medium of photon-matter interaction for its wide optical transparency in the visible wavelength range as well as its highly efficient photothermal conversion for tuning the focal length.

Experimentally, the physiochemical, optical absorption, and temporally photothermal properties of $CsWO_3$ NPs as well as the thermo-mechanical and -optic properties of the PDMS fluidic lens were examined. The physical characteristics of the $CsWO_3$ NP solution-based PDMS lens including the monitored profiles of the photothermally induced temperature and the temperature-dependent variable focal length as a function of optical power density were determined, and the optical properties of the fluidic lens, such as the front focal length, quality of the focused beam and the diameter size of the focused beam, were empirically characterized. Subsequently, the fluidic lens was cascaded with an aspheric condenser lens to act as a converging detection objective lens in the detection arm of a LSFM for the assessment of the lens' focal tunability by imaging the fluorescence version of the $CsWO_3$ NPs embedded in the PDMS matrix.

2. Materials and methods

2.1. Preparation and characterization of the $CsWO_3$ NP solution

The $CsWO_3$ micro(μ) powder used in this study was purchased from Justnano Corporation of Taiwan. To obtain the $CsWO_3$ NP solution, 10 g of the $CsWO_3$ micro(μ)powder and 600 g of zirconia beads of 0.1 mm diameter were placed in a grinding bowl, which was then filled up with a proper volume of DI water. The grinding bowl was then securely installed in the chamber of a wet-grinding machine (Justnanotech Co., Taiwan) for a 4-hour (h) grinding process set at a speed of 2200 rotations per minute (rpm) alongside the system temperature set at 15 °C. Afterward, the 4-h grinding process was repeated with the same grinding speed and system temperature using 0.05 mm zirconia beads, and a solution bath of 60 nm $CsWO_3$ NPs was produced at a concentration of 25 mg mL^{-1}, which can be further diluted to amend for the experimental use.

2.2. Transmission electron microscopy

A transmission electron microscope (JEM-1400, JEOL, Japan) was used to observe the morphology and the particulate size of the NPs. To prepare the sample, the NP solution was diluted, dropped onto a carbon-coated copper grid, dried at ambient temperature, and installed in the sample chamber for image acquisition.

2.3. X-ray diffraction

An X-ray diffraction (XRD) instrument (D2 phaser, Bruker, USA) was used to examine the crystalline lattice of the NPs by irradiating them with X-ray in the angular range from 0° to 80°, where the peaks of the characteristic diffraction can be determined. To record the XRD spectrum of the NPs, the NP solution was dropped onto a 1 cm × 1 cm glass substrate, left to dry in an aerated chemical hood, and placed in the chamber.

2.4. Dynamic light scattering

Analysis of the hydrodynamic feature size of the NPs was performed using a dynamic light scattering instrument (Delsa-Nano C, Beckman Coulter, USA). With the NP solution purified using a centrifuge machine and loaded into a quartz cuvette, the hydrodynamic size of the NPs was quantified according to the speed of Brownian motion of NPs in the solution, of which a laser beam scattered when irradiated upon the NPs.

2.5. UV-VIS absorption spectroscopy

To measure the optical absorbance spectra of the $CsWO_3$ NP solution, a PDMS cuvette was made in resemblance of the size of the standard plastic cuvettes, sequentially filled with an array of NP concentration, 0.5 mg mL^{-1}, 1 mg mL^{-1} and 2 mg mL^{-1}. By inserting the solution-filled cuvette into the sample chamber of the UV-VIS spectroscopy (UV-1800 Shimadzu, Japan), the absorption spectra of the samples in the wavelength range from 350 nm to 1100 nm can then be recorded.

2.6. Tensile strength measurement

The tensile test of ASTM D638, which measures the required force as well as the spatial extent to which the elongated sample's breaking point is reached, was used to measure the temperature-dependent Young's modulus of the PDMS, defined as stress over strain in N cm^{-2}. As shown in Fig. 4(a) and (b), the mold of the testing sample was designed in SolidWorks and fabricated using a laser curing 3D printer, according to the ASTM D638 method's guideline on the dimensions and shape of the testing samples. To fabricate the PDMS samples, siloxane A and cross-linker/curing agent B in a ratio of 10/1 was evenly mixed and then put into a 3D printed mold. After vacuuming to evacuate all air bubbles, the sample was thermally annealed for 1 hour and taken out of the mold after grafting. By attaching a strain gauge to the PDMS sample and securely mounting the PDMS sample on the clamps, the PDMS sample was stretched from both ends with a finite amount of force until a fracture in the sample occurs, while heating was constantly applied in the sample's surrounding environment at 25 °C, 34 °C, and 48 °C, and the extended strain was monitored by the strain gauge.

2.7. Design and fabrication of the PDMS fluidic lens

In principle, the dimensions of the fluid chamber and lens frame were designed for the necessary amount of $CsWO_3$ NP solution to photothermally induce changes in the refractive index and the curvature of lens surface for the focus-tuning and to accommodate the standard holder of 1 inch diameter lens. This PDMS lens is constructed with 2 separate lens pieces, namely, a plano-convex lens and a meniscus, which, when bonded together, form a fluidic chamber for filling the NP solution. In the second step (2) of the fabrication flow shown in Fig. 1, the overall dimension of a polypropylene (PP) mold, which has a radius of curvature of 15.3 mm for stamping out the lens surfaces of both lens pieces, is presented. While the plano-convex lens has a diameter of 25.4 mm and a thickness of 6 mm, the meniscus was designed with an average thickness of 3 mm and a height of 8 mm to reserve a chamber volume of 1.047 cm^3, making the mechanical property of the lens more uniform. A polydimethylsiloxane (PDMS) silicone elastomer (SYLGARD™ 184, Dow Chemical, USA) was used to fabricate the lens frame, due to its optical transparency, low polymerization temperature, moldability as well as great stability and flexibility after the curing process in the temperature range of −50 °C to 200 °C.[18]

As can be seen in Fig. 2, appropriate amounts of siloxane A and cross-linker/curing agent B in a ratio of 10 : 1 (base : curing agent) were first mixed and then stirred thoroughly. A proper amount of the mixed PDMS was then poured into the PP mold at the designated height (6 mm) to make a plano-convex lens, and a heat-resistant glass ball (20 mm in diameter) held tightly by a position-adjustable bracket was dipped directly into the center of a second PP mold for producing a meniscus lens structure that has a cavity for micro-injecting the $CsWO_3$ NP solution into the fluidic chamber. Afterward, the PDMS-filled

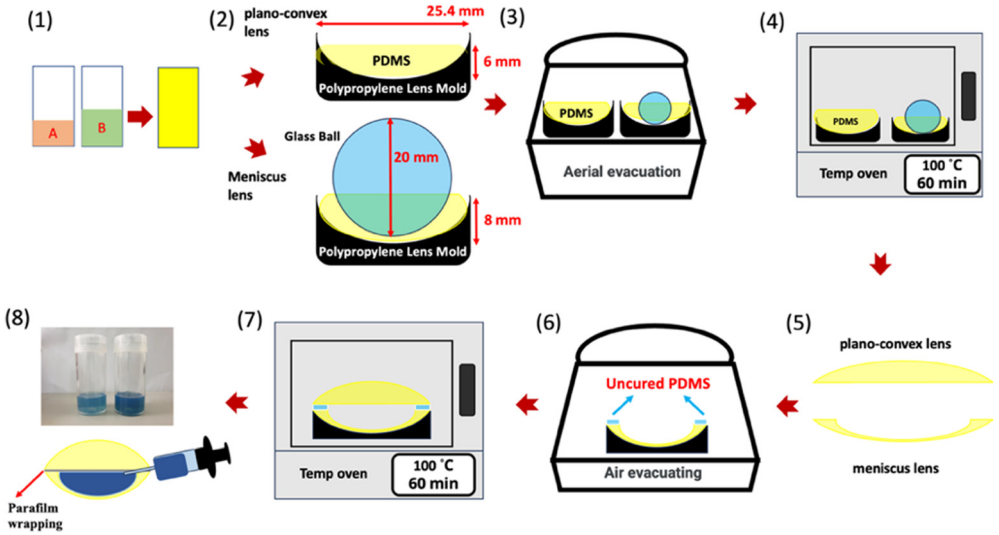

Fig. 2 Design and fabrication of the $CsWO_3$ NP solution-incorporated PDMS fluidic lens. A flow of the fabrication processes of the PDMS lens in a series of (1) PDMS preparation, (2) molding, (3) vacuuming, (4) thermal annealing, ((5), (6) and (7)) lens bonding, and (8) NP solution-filling processes is presented.

molds were aerially evacuated in a vacuum chamber for an hour to remove air bubbles. Once the vacuuming was done, the PDMS-filled molds were removed from the vacuum chamber and put into a high-temperature oven for 1 h of the thermally curing process at 100 °C. Once completed, the meniscus and the plano-convex lens were taken out of the molds. Similarly, an uncured, vacuumed PDMS mixture was applied on the rim of the plano-convex lens, bonded with the meniscus and thermally annealed at 100 °C for an hour to seal these two lens pieces. The $CsWO_3$ NP solution of 1 mg mL^{-1} was then slowly syringe-injected into the cavity of the assembled lens, and the cemented edge of the two lens pieces was wrapped with a parafilm to strengthen the lens' structure.

2.8. Light sheet fluorescence microscopy

Fig. 3(a) illustrates the implementation of the $CsWO_3$ NP-incorporated PDMS lens (NPPL) as a focus-tuning element in conjunction with a condenser lens (CL) to compose a converging detection objective lens in a light sheet fluorescence microscope (LSFM). Central to the LSFM is a broadband white light laser (SuperK EXTREME EXU-6, NTK Photonics, Denmark) that illuminates the entire excitation arm. The white laser beam was first filtered through a 468 nm fluorescence filter (25 nm in bandwidth) to produce a blue laser beam, beam-expanded by a cascade of AS1 and AS2 lenses and focused by a cylindrical lens (CYL) to form a sheet of light. The light-sheet was then further narrowed by a 10× air objective lens with a numerical aperture

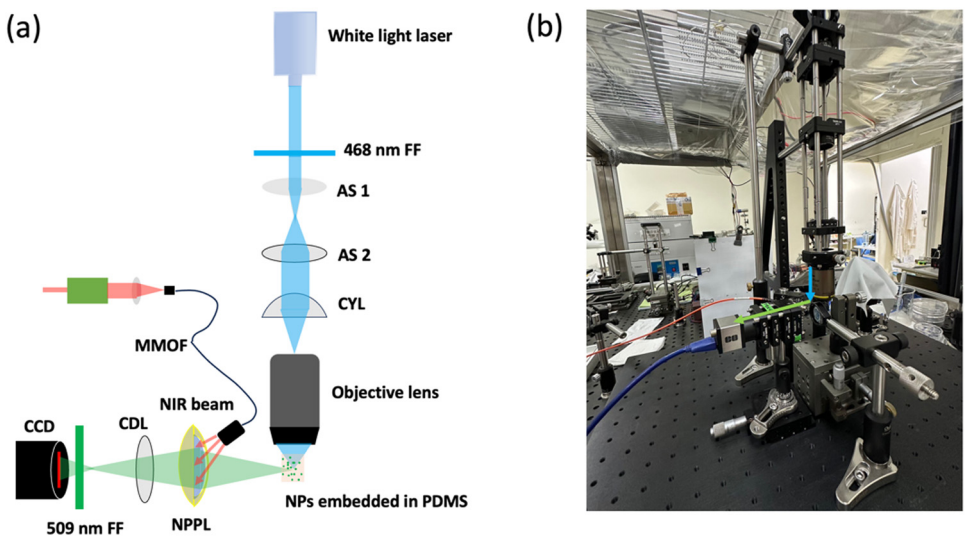

Fig. 3 Light sheet fluorescence microscopy. (a) A schematic of the component-level setup of the fluidic lens-incorporated LSFM system and (b) the actual experimental setup. MMOF, AS, CYL, CDL, CCD and NPPL stand for multi-mode optical fiber, aspherical lens, cylindrical lens, condenser lens, charge coupled device, and the $CsWO_3$ NP solution-incorporated PDMS lens, respectively.

of 0.3 (Nikon, Japan) for sample interrogation. Upon excitation by the illuminating beam, the fluorescence image signal emanating from the fluorescent samples was collected by the converging detection objective lens and projected onto the sensor surface of a CCD camera for image registration. The PDMS lens was then side-illuminated with the diverging NIR laser light from the MMOF to vary the focal length of the fluidic lens as well as the working distance of the detection objective lens to image the fluorescein-coated $CsWO_3$ NPs. Side-illumination was implemented to avoid the necessity of the dichroic component that reduces the intensities of both NIR illumination and fluorescence signals. A photo illustrating the actual set up of the LSFM is also presented in Fig. 3(b), where the beam directions for excitation and detection are shown in blue and green arrows, respectively.

3. Results and discussion

3.1. Stoichiometric characterization of $CsWO_3$ NPs

To commence the study, the stoichiometric properties of $CsWO_3$ NPs including the morphological contour, shape, feature sizes, crystalline structure, optical absorbance and photothermal properties were analyzed using a transmission electron microscope (TEM) (JEOL 1400, Japan), an X-ray diffractometer (D2 Phaser, Bruker, U.S.A.), a dynamic light scattering instrument (DelsaNano C, Beckman Coulter, U.S.A.), a visible-near-infrared (VIS, NIR) absorbance spectrometer, and an NIR laser-incorporated temperature measurement setup, correspondingly. Fig. 4(a) illustrates the TEM image of the dried $CsWO_3$ NPs deposited on the carbon-coated copper mesh, showing the particulate surface contour, shape and feature size, a statistical distribution of which is shown in the inset histogram of Fig. 4(b). To examine the crystalline structure of the $CsWO_3$ NPs, the XRD spectrum of the NPs was recorded, and is shown in Fig. 3(b), which reveals the remaining diffraction peaks at (002), (102), (200), (112), (202), (212), (004) and (204), while other visible XRD peaks observed for the $CsWO_3$ powder, such as (220), (222), (400), and (224) according to the spectrum of censium tungstate micropowder ofthe Joint Committee on Powder Diffraction Standards (JCPDS) card No. 83-1334 were diminished. Likewise, the optical absorbance spectra of the $CsWO_3$ NPs were recorded using an ultraviolet-visible (UV-VIS) spectrophotometer equipped with UV-probe 2.43 software (UV-1800 Shimadzu, Kyoto, Japan), which is housed in an air-conditioned environment at 26 °C. To carry out the photo-absorption measurement, the lab-made PDMS cuvettes were filled with the NP solutions of the designated concentrations, namely, 0.5 mg mL^{-1}, 1 mg mL^{-1} and 2 mg mL^{-1}, and loaded in the sample chamber of the spectrophotometer, and the absorption spectra were recorded and are presented in Fig. 4(c). While the 0.5 mg mL^{-1} and 1 mg mL^{-1} NP solutions retained at least 90% optical transparencies (with respect to the lowest absorbance points) from 411 nm to 731 nm and from 468 nm to 615 nm, respectively, 2 mg mL^{-1} allows 80% optical transparency for merely 67 nm wavelength bandwidth. To further determine a proper NP concentration, the temporally dependent course of temperature profiles of the NIR laser-irradiated NP solution as a function of concentration are depicted in Fig. 4(d), where the saturation temperatures of

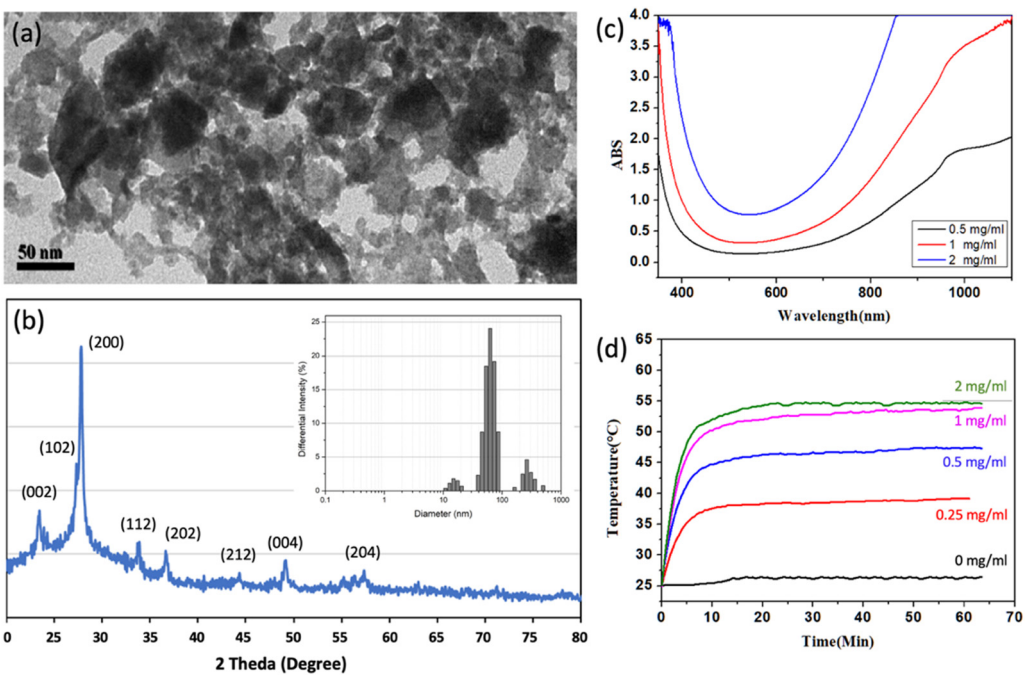

Fig. 4 Stoichiometric properties of $CsWO_3$ NPs. (a) TEM images of the NPs' contour profile and shape. (b) XRD spectrum the NP's crystallinity. (c) Optical absorbance and (d) temporally dependent increase in temperature as a function of the NP concentration. Optical power density used in (d) is 124 mW cm^{-2}.

0 mg mL^{-1}, 0.25 mg mL^{-1}, 0.5 mg mL^{-1}, 1 mg mL^{-1} and 2 mg mL^{-1} plateaued correspondingly at 26.2 °C, 39.1 °C, 47.4 °C, 54.1 °C and 54.7 °C when the thermal equilibrium between the solution and the ambient environment was reached. As can be seen from Fig. 4(c) and (d), although 2 mg mL^{-1} NP solution attained the highest saturation temperature, its optical transparency retains less than 80% for all visible wavelengths, undesirable to making the lens for fluorescence imaging. However, 1 mg mL^{-1} NP solution not only can achieve a similar saturation temperature as the one of 2 mg mL^{-1}, but also possesses a sufficient range of transmissive wavelengths to accommodate both sample excitation and fluorescence signal extraction, and is, therefore, chosen to construct the fluidic lens.

3.2. Thermo-mechanical analysis of poly-dimethylsiloxane (PDMS)

The thermo-mechanical property of PDMS materials was quantified by the ASTM D638 tensile test that measures the material's Young's modulus, which is defined as the applied stress over the displaced dimension along the direction of the sample's physical length. The preparation of the testing specimen was carried out by drawing a 3D schematic of mold design (Fig. 5(a)) in the SolidWorks software and fabricating a mold using a 3D printing machine (Fig. 5(b)), and a PDMS specimen was made by the same method outlined in the Materials and Method section. Afterward, the PDMS specimen was attached on a tensile gauge (Fig. 5(c)), securely mounted with the clamps of the computerized tensile tester on both ends of the specimen and stretched with an incremental force while keeping the designated temperature of the surrounding environment at 25 °C, 34 °C and 48 °C, which was chosen for its close proximity to the saturation temperature of 1 mg mL^{-1} NP solution, until a fracture in the specimen occurs. Fig. 5(d) depicts the stress–strain curves, where the variation in the slopes of the temperature-dependent fitting lines is apparent, and Young's moduli of the PDMS material at 25 °C, 34 °C and 48 °C, which are chosen to match the saturation temperature of 1 mg mL^{-1}, are 6.33 MPa, 4.5 MPa and 3.97 MPa, correspondingly. This decreasing trend of the modulus values suggests the higher mechanical flexibility of the PDMS material when the ambient temperature is higher. Such property is highly dictated by the thermal annealing temperature in the fabrication process and indicates suitability of the NIR-irradiated $CsWO_3$ NP solution as a heating source to inducing the thermo-expansion and thermo-optic effects in PDMS materials.

3.3. Photothermal properties of the $CsWO_3$ NP solution-incorporated fluidic lens

Fig. 6(a) emulates the focusing of a collimated laser beam by the $CsWO_3$ NP solution-incorporated fluidic lens and presents the illustrative terms used in the following analysis of the lens' front focal length (FFL), including the radius of curvature (R), lens thickness (d), and height (H). To verify the sufficiency of the thermal energy generated by the photothermal effect of the NIR-irradiated $CsWO_3$ NP solution in modulating the lens' focal length the time-course profiles of temperatures of the external surface of the lens filled either with the $CsWO_3$ NP solution or water, and of the $CsWO_3$ NP solution in the fluid chamber were examined and are shown in Fig. 6(b). As can be seen from the figure, when the temperature of the $CsWO_3$ NP solution hiked up to the saturated temperature of 44.1 °C, the temperature of the fluidic lens' surface plateaued at 39.7 °C which garners 4.4 °C in difference and stands in a stark contrast with the surface temperature of the lens filled with deionized (D.I.) water (25 °C). The saturated temperature of the lens frame at 40 °C indicates Young's modulus value between 4.5 MPa and 3.97 MPa and implies that the optical index of refraction (n) and R of the fluidic lens can be thermally modulated *via* the NP's photothermal conversion.

3.4. Numerical analysis of PDMS lens' variable focal length

To compute the front focal length (FFL) of the PDMS lens, the lens maker's equation that accounts for the thickness of a lens

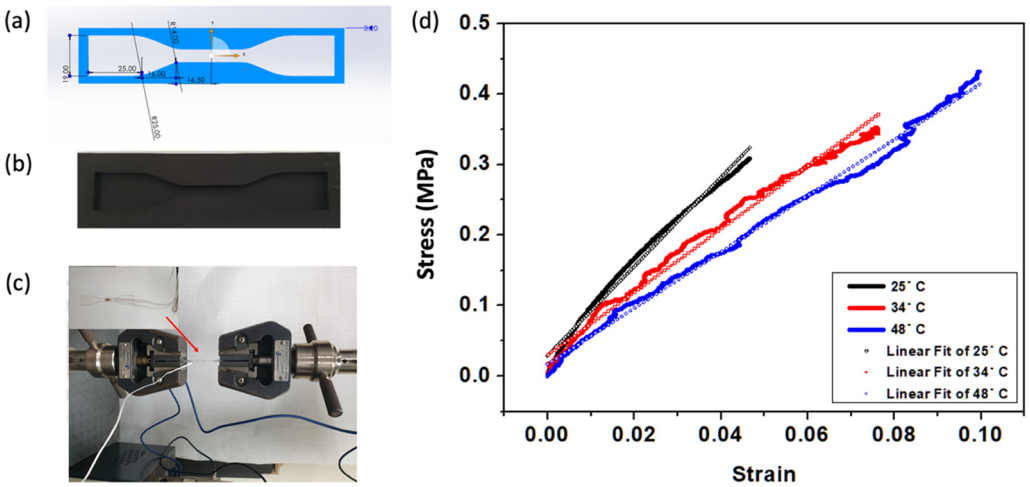

Fig. 5 Thermo-mechanical properties of PDMS. (a) Solidwork design, (b) 3D printed mold and (c) PDMS specimen attached to a strain gauge for the tensile test, and (d) the stress–strain plots with linearly fitting lines as a function of ambient temperature are presented.

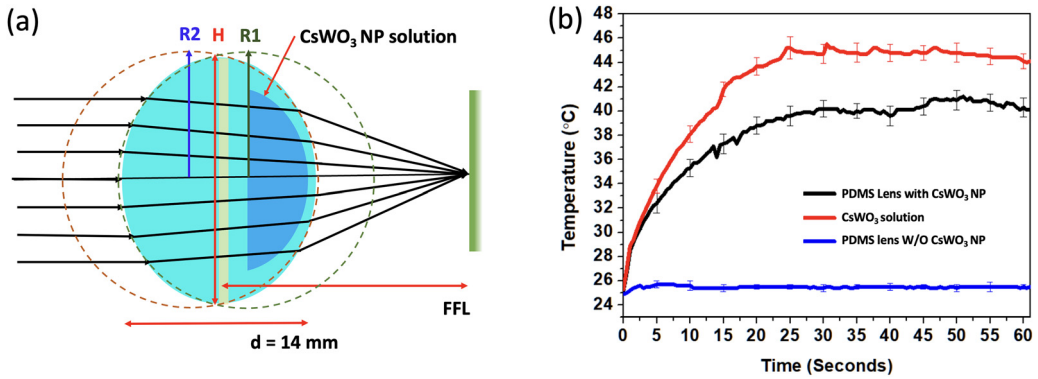

Fig. 6 (a) Schematic of the focusing of the fluidic lens when illuminated with a collimated laser beam, (b) the time-dependent temperature profiles of the surface of the lens filled with the $CsWO_3$ NP solution or water as well as of the $CsWO_3$ NP solution in the fluidic chamber are illustrated. R_1 and R_2, d, H, and FFL stand for the radii of curvature of the lens' front and back surfaces, the lens' thickness, height and the front focal length, respectively; the NIR optical power used for the time-dependent temperature measurement is 261 mW. N = 3 for all traces in (b).

was used in the following analysis and is expressed as follows:[19]

$$\frac{1}{f} = (n-1)\left(\frac{1}{R_1} - \frac{1}{R_2} + \frac{(n-1)d}{n \cdot R_1 \cdot R_2}\right) \quad (1)$$

where f, n, R_1 and R_2, and d are the front focal length, the optical index of refraction of the PDMS material, the radii of curvatures of the lens' front and back surfaces, and the thickness of the lens, correspondingly. Since the PDMS material used in this study is well known for its thermal expansion and thermo-optic effects which vary n and $R1$ simultaneously, the temperature dependence of n and R_1 needs to be experimentally extracted. R_2 is 15 mm remaining intact since it is not influenced by the NIR illumination.

On the one hand, the thermo-optic effect quantified with the temperature-dependent n was computed by empirically measuring the change in the surface temperature of the PDMS lens, ΔT, using a thermometer (TD-4C, Yotec, Taiwan) when the PDMS lens was irradiated with an array of NIR optical power densities, namely, 0 mW cm^{-2}, 51 mW cm^{-2}, 80 mW cm^{-2}, 155 mW cm^{-2}, and 226 mW cm^{-2}, using the following formula:

$$n = n_0 + \Delta T\left(\frac{dn}{dT}\right). \quad (2)$$

where n_0, the refractive index of PDMS at room temperature, is $\sim$ 1.43 measured by an ellipsometry (Alpha-SE, J.A. Woollam Co., U.S.A.), and dn/dT, the thermo-optic coefficient, is $\sim -4.5 \times 10^{-4}$/°C.[20] The variation in n as a function of ΔT can then be computed accordingly and presented in Fig. 7(a), where n decreases as the lens' surface temperature increases from 25.1 °C to 61.4 °C. The details of the lens' surface temperature as a function of the NIR optical power densities are shown in Table S1 of the SI. Subsequently, with the computed n and known constants, R_1 = 15.29 mm (determined by ImageJ) and R_2 = 15 mm (Specified by the vendor) and d = 14 mm, the FFL attributed to the thermo-optic effect can be computed and presented by the black line in Fig. 7(d). On the other hand, the thermal expansion effect of the fluidic lens upon NIR irradiation was characterized by the measurement of R_1 and d, utilizing a brightfield stereoscope (SMZ745T, Nikon, Japan) equipped with a CCD camera. To determine the photothermally variable R_1 and Δd of the lens, the images of the lens' surface contour when irradiated with an array of the NIR optical power densities were acquired and analyzed using a built-in function, "Kappa-curvatures", in the ImageJ software (National Institutes of Health, U.S.A.). The raw images of the lens' surface contour are presented in Fig. S1 of the SI. Fig. 7(b) and (c) show the respective decreasing and increasing trends for R_1 and Δd of the lens as the lens' surface temperature is increased, of which the respective minimal and maximal values at 226 mW cm^{-2} are 13.2 mm and 25 μm.

With the photothermally variable R_1 and Δd determined for each optical power density, the FFL attributed to the thermo-expansion effect can be subsequently quantitated and is presented by the blue line in Fig. 7(d). Note that since the thermo-optic and thermo-expansion effects have an opposing nature in the variation of the FFL, with the former one elongating and the later one shortening, the synergy of both effects on the lens' FFL allows for the determination of the theoretical FFL of the fluidic lens as a function of NIR power densities (Table S1 in the SI), which is represented by the red dots of Fig. 7(e), exhibiting a shortening trend as the illuminating optical power intensity increases and closely aligning with the experimental values shown in orange and light green dots within 10% of deviation. The fluidic lens exhibited a highly reliable tuning of the focal length but temporally took averages of 5 min, 16 min, 20 min, 25 min, 5 min, 3 min, 2 min, and 1 min on the corresponding forward and backward traces to reach the designated focal length. To demonstrate the durability, repeatability and reliability of the $CsWO_3$ NP solution used in this study as a medium that provides heat for thermo-optic and thermo-expansion effects in poly-dimethylsiloxane upon NIR irradiation, the optical absorbance and morphology of the NPs before and after 60 complete cycles of heating and cooling from 0 mW cm^{-2} to 226 mW cm^{-2} (with 3 power densities, 51 mW cm^{-2}, 80 mW cm^{-2}, 155 mW cm^{-2} in between) and back to 0 mW cm^{-2} were examined using a visible (VIS)-near-infrared (NIR) spectrophotometer and a tunneling electron microscope (TEM),

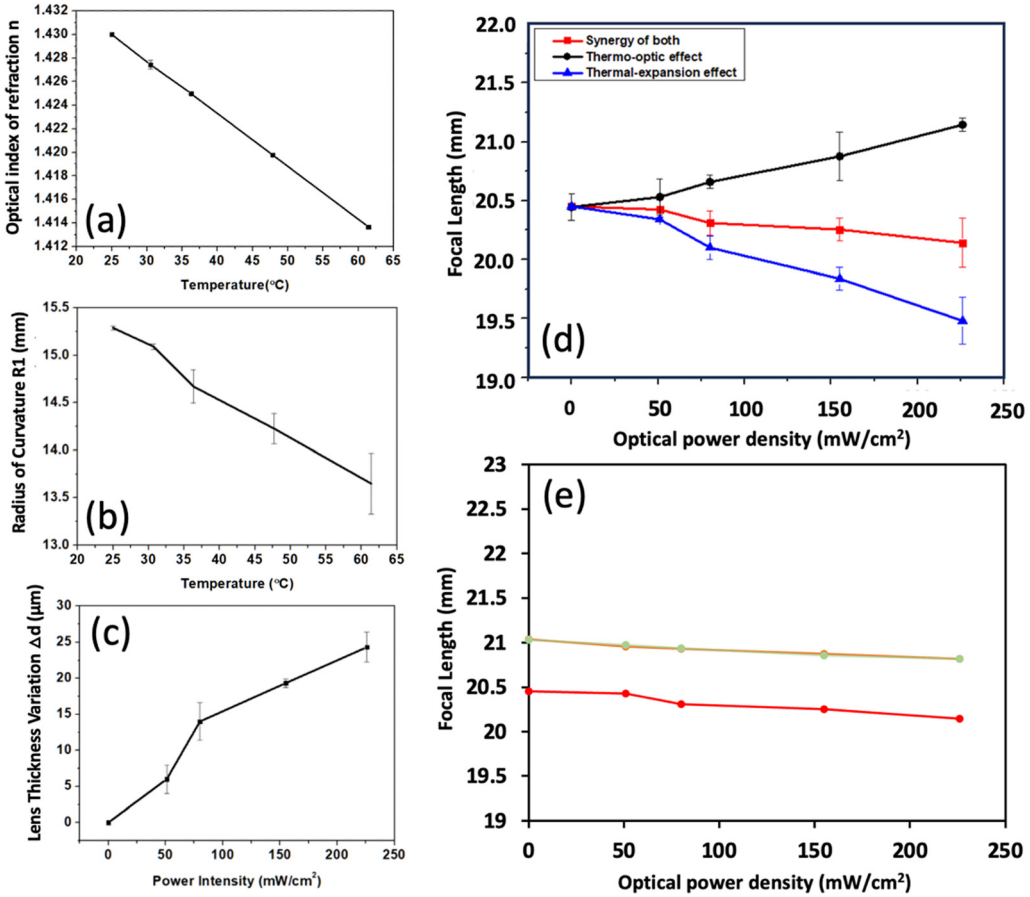

Fig. 7 Optical properties of the $CsWO_3$ NP-incorporated fluidic lens. (a) Computed optical index of refraction, n; (b) measured radius of curvature, R_1; (c) variation in measured lens thickness, Δd; and (d) the theoretical front focal length (FFL) of the photothermal lens pertaining to the thermal expansion and thermo-optic effects as well as their synergy, and (e) the theoretical and experimental values of the FFL as a function of NIR power densities (interchangeably with the lens' surface temperature) are presented. The orange and light green data points in e are the average experimental values of 60 heating and cooling cycles when the NIR power density, respectively, traversed from low (0 mW cm^{-2}) to high (226 mW cm^{-2}) and then back to low (0 mW cm^{-2}). Error bars in (a)–(d) are derived with N = 3, and the error bars of orange and light green traces, which are barely discernible, in (e) are derived with N = 60.

respectively, and the focal length of the heating/cooling cycles was measured and analyzed. It was found that the traces of optical absorption spectra of the NPs before and after the repeated NIR exposure varied slightly due to water evaporation in the fluidic chamber, which renders a higher NP concentration, and the corresponding higher optical absorbance, as shown in Fig. S3, therefore, necessitates a constant re-filling water before carrying out experiment. The corresponding TEM images of the NPs shown in Fig. S4 depict the NPs' morphology and feature sizes before and after the heating/cooling cycles, which remain largely unaltered. Moreover, the standard deviations of the focal length at optical power densities of 0 mW cm^{-2}, 51 mW cm^{-2}, 80 mW cm^{-2}, 155 mW cm^{-2}, and 226 mW cm^{-2} in the forward tuning are within ±0 mm, ±0.00816 mm, ±0.01211 mm, ±0.02137 mm, and ±0.02338 mm, respectively, and the standard deviations of the focal length at optical power densities of 226 mW cm^{-2}, 155 mW cm^{-2}, 80 mW cm^{-2}, 51 mW cm^{-2}, and 0 mW cm^{-2} in the backward tuning are ±0.00764 mm, ±0.00816 mm, ±0.01118 mm, ±0.017 mm, and ±0.02134 mm, respectively, implying that the optical and mechanical properties remain robust and functional. However, the transmittance was decreased from 70% to 60% in almost 1.5 years, which suggests a long-term degradation of the optical transparency of PDMS over time and may require an additional coating to prevent oxidation in air. In comparison with other focus-tunable lenses, which is presented in Table S2 of the SI, enabled with other actuation schemes including electromagnetic, liquid crystal, thermo-pneumatic, and electrowetting means, one can immediately see that most of the schemes require physical inputs of voltage and electric power except the photothermal scheme. The electrowetting and electromagnetic actuation require at least 20 volt with the tuning range of the focal length on the scale of tens of millimeters (mm) and response time in tens of milliseconds, whereas the liquid crystal lens requires the least input voltage alongside a large tunable range and quick response. In addition, the thermo-pneumatic scheme not only requires 300 mW of electro-thermal energy, but also enables a smaller tuning range in

millimeters and a longer time response in seconds. One of the biggest advantages of the photothermal scheme is its non-contact actuation, which allows applications where NIR-based auto-adjustment, non-physical contacts and hazard-free tasks are necessitated. Long response time and short tuning range can be further improved by implementing several strategies such as adjustments of the ratio of siloxane A and cross-linker B and of the annealing temperature and time, reduction of the thickness of the lens frame, optimization of the NP concentration or application of the high-intensity NIR pulse beam may be instrumental in speeding up the response of the lens.

To address the question of whether the NPs are well distributed in the lens chamber, the NPs are coated with a layer of fluorescein, which is a bright green dye, filled in the lens chamber and illuminated with a diameter-expanded blue excitation beam while being side-irradiated at 226 mW cm^{-2} NIR power density. In Fig. S5, the fluorescence images of the NP solution filled in the lens chamber before and after NIR irradiation for up to 60 cycles of heating and cooling are shown, which illustrates great and similar uniformity of the suspended NPs in the solution after a prolonged exposure to NIR irradiation, and these NPs are well separated in the solution due to electro-static repelling forces.

3.5. Optical characterization of the fluidic lens

To characterize the beam quality and focusing ability of the fluidic lens, a blue laser beam was beam-expanded, collimated and focused by the lens onto a CCD camera for display of the

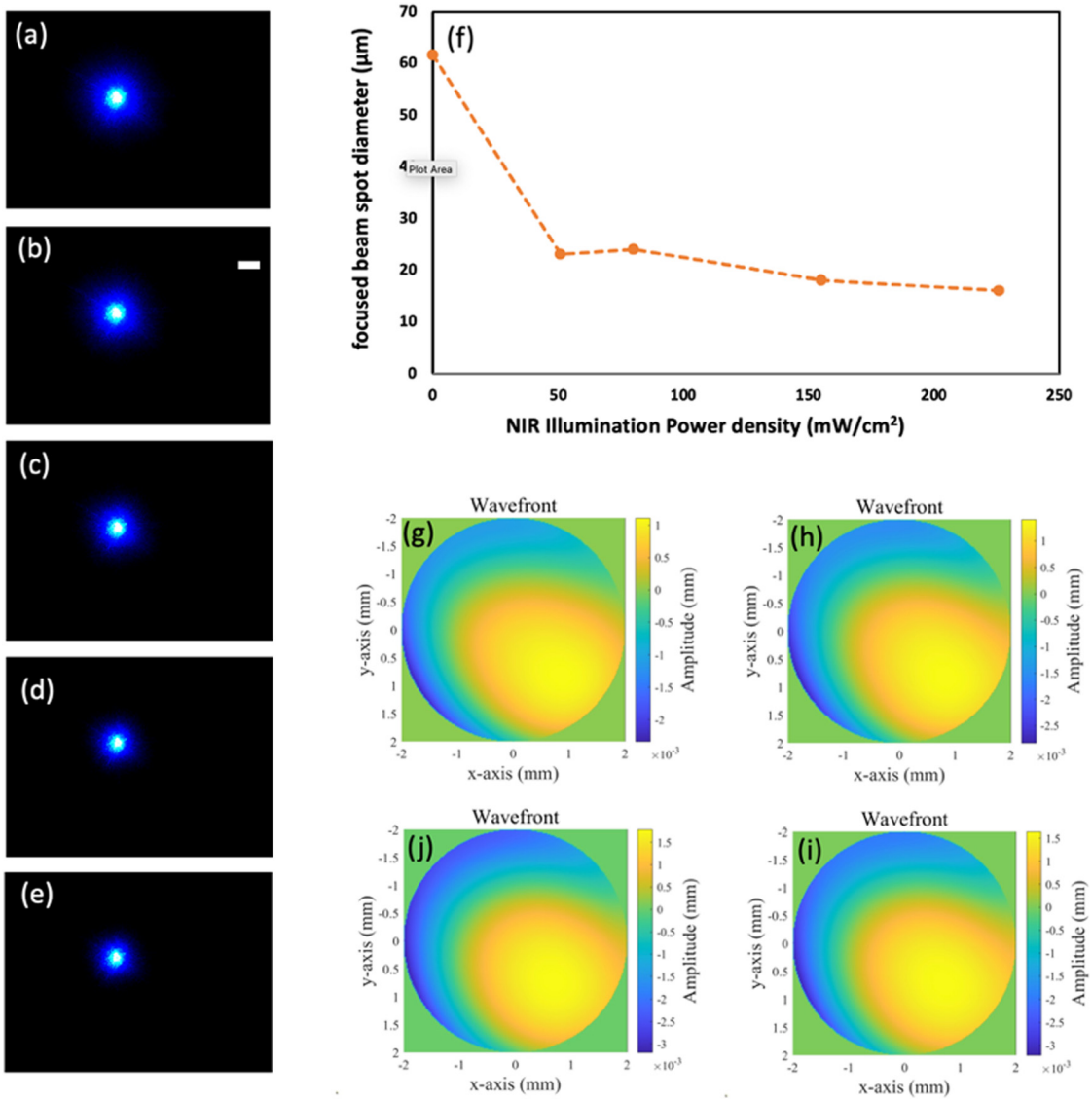

Fig. 8 Focusing property and optical aberration of the fluidic lens. Images of variable focal spots of the lens when side-illuminated with an array of NIR optical power densities: (a) 0 mW cm^{-2}, (b) 51 mW cm^{-2}, (c) 80 mW cm^{-2}, (d) 155 mW cm^{-2}, and (e) 226 mW cm^{-2}. (f) Their respective spot diameters and phase front images of the lens arranged in clockwise order when irradiated with 51 mW cm^{-2} (g), 80 mW cm^{-2} (h), 155 mW cm^{-2} (i), and 226 mW cm^{-2} (j) starting at the upper left-hand corner. The incident optical power at the imaging plane is 158 μW; N = 3 for the measurement of the focused beam spots in (f).

focused spot as a function of the side-illuminated NIR optical power densities shown in Fig. 8(a)–(e). Also presented in Fig. 8(f) is the decreasing diameter of the concentric focused spots as a function of the increment NIR power density while the sphericity of the focused beam spot remains intact. Subsequently, the aberration of the fluidic lens as a function of the NIR power density was examined using a wavefront sensor that was set up to acquire images of the phase front and compute the parameters of Zernike polynomial, and this work is under preparation for a separate manuscript. By analyzing the acquired images shown in Fig. 8(g)–(j), it was found that tilt *x* (Z1), defocus (Z3), and astigmatism (Z5) are more dominant parameters as they undergo large changes in amplitude, and can vary from 2.57×10^{-4} μm to 4×10^{-4} μm, -2.37×10^{-4} μm to -3.8×10^{-4} μm, and 1.23×10^{-4} μm to 1.07×10^{-4} μm, respectively, as the NIR power density increases from 0 mW cm^{-2} to 226 mW cm^{-2}, which may be useful for the fine-tuning of the aberration-induced phase shift for phase-sensitive applications like optical coherence tomography.

3.7. LSFM imaging of fluorescent powder and fCsWO$_3$ NPs

Thereafter, the fluidic lens was positioned in a cascade with a condenser lens 33 mm apart, acting as an objective lens in the detection arm of the LSFM system, as shown in Fig. 1(b) and (c), to acquire the fluorescence images of samples. The working distance of the detection arm, as presented in Fig. S2 of the SI, varies from 0.46 mm to 0.61 mm as the NIR power density increases from 0 mW cm^{-2} to 226 mW cm^{-2}, implying the reduction of the focal length, depth of field and field of view; also shown on the same figure is the transmission efficiencies of the fluidic lens at all optical power densities, where the maximal transmission efficiency garners 69.36% with no more than 3% deviation. Fig. 9 presents the LSFM fluorescence images of the fluorescein-coated $CsWO_3$ fNPs at 20 mg mL^{-1} (a)–(e) and fluorescent powder (f)–(j) to demonstrate the tunability of the fluidic lens *via* NIR irradiation. It is quite pronounced that the density of the fluorescent μpowder granules varies from low (Fig. 9f) to high (Fig. 9j) as the lens' focal plane decreases because the increase in numerical aperture of the objective lens not only minimize the focal volume but also concentrate excitation photons in a smaller region, thus increasing the image contrast. Fig. 9(k)–(o) and (p)–(t), respectively, present the zoomed-in LSFM images of the fCsWO$_3$ NPs within the red dotted rectangles 1 and 2 in Fig. 9(a),

where unique features of the NPs undergo contrast enhancement as the NIR power density increases. One can easily see that the improvement in the detection arm's optical resolution sharpens the contrast of individual NPs (k–o, p–t) which become increasingly discernable as the NIR power density peaks.

To analyze the effectiveness of the lens' varying focal length on enhancing the image contrast, the spatially dependent fluorescence intensities along white lines drawn across two

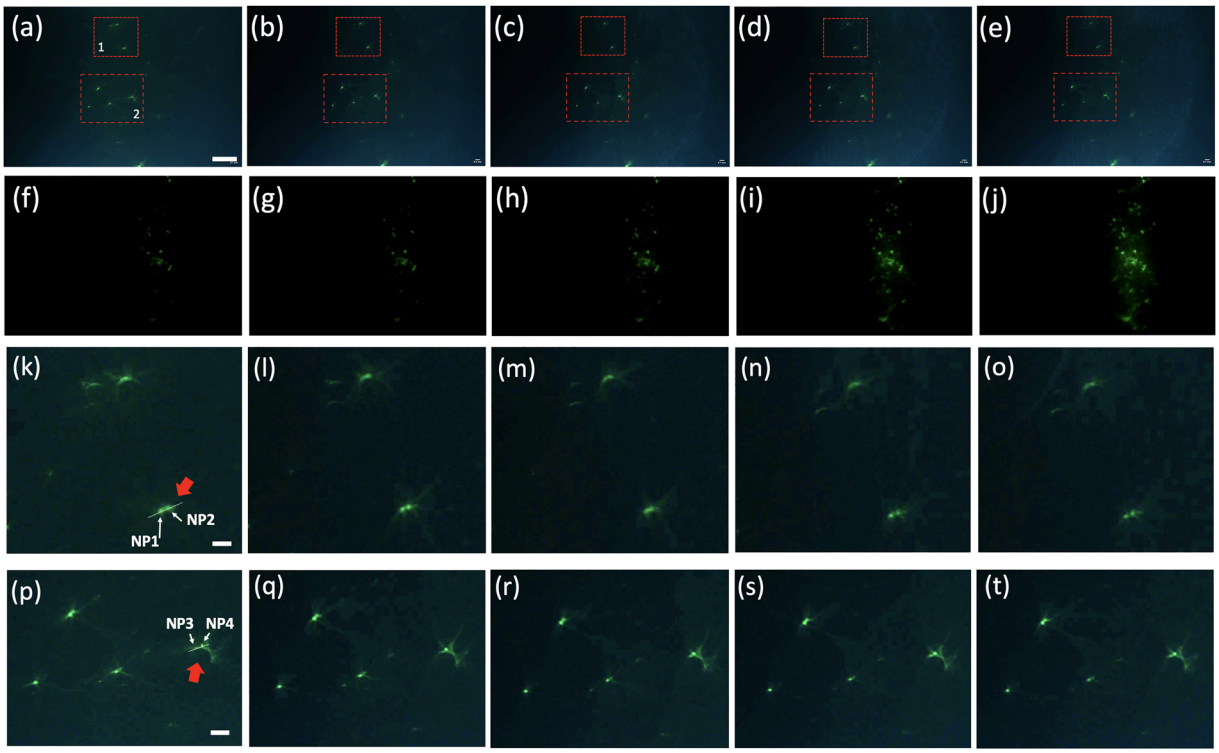

Fig. 9 LSFM images. Fluorescence images acquired with fCsWO$_3$ fNPs (a)–(e), green fluorescent powder (f)–(j) and the magnification of red dotted rectangles 1 (k)–(o) and 2 (p)–(t) denotated in (a) as a functionof NIR power density, 0 mW cm^{-2}, 51 mW cm^{-2}, 80 mW cm^{-2}, 155 mW cm^{-2} and 226 mW cm^{-2} are depicted. Incident excitation power at the focal plane is 5.13 mW; the corresponding scale bars in the first and second, and third and fourth rows are 500 μm (a)–(j) and 100 μm (k)–(o).

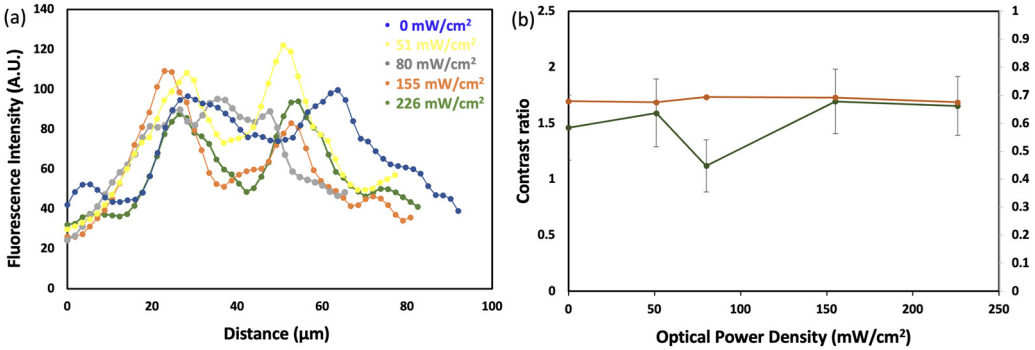

Fig. 10 Analysis of image contrast. (a) An example of dataset of fluorescence intensities drawn across a pair of two fCsWO$_3$ NPs from the dotted rectangle 1 shown in Fig. 9(a) and (b), the optical transmittance of the photothermally tunable lens (in brown), and the average contrast ratios of NPs alongside the standard deviations (in dark green) are presented. The numbers of experimental measurements for the optical transmittance and for computing the contrast ratio of the NPs are N = 3 and N = 4, respectively.

pairs of NPs are shown in Fig. 9(k) and (p), where, as an example, the raw data of Fig. 9(k) as a function of NIR power density are plotted in Fig. 10(a). The contrast ratios of the NPs were deduced by dividing the highest fluorescence intensity of the NPs over the lowest fluorescence intensity between the NPs, and it can be observed in Fig. 10(b) that the average contrast ratio of 4 individual NPs increases as the power density increases and tops at 226 mW cm^{-2}. Note that although the overall system contrast is enhanced due to the increase in the detected fluorescence intensities, the nominal size of individual NPs is 60 nm which cannot be revealed optically from these images since the pixel dimensions of the CMOS sensor in the camera are 2 μm × 2 μm, and the spatial and axial resolutions of the lens are on the scales of micrometers (μm) (Fig. 8(f)).

In summary, this study introduced a plasmonic NP solution-based fluidic lens, the front focal length of which varies as the lens is side-illuminated with the incremental NIR optical power density. Specifically, the stoichiometry of the CsWO$_3$ NPs and the photothermal properties as well as the optical properties of the NP solution-incorporated PDMS lens were characterized, and the lens was successfully incorporated in the detection arm of a custom-built LSFM to image green fluorescent micropowder and the fluorescein-coated CsWO$_3$ NPs, where the sharpened image contrast in discriminating individual NPs was demonstrated. This fluidic lens can be further implemented in other optical microscopy systems, where fine adjustments of the focal plane in a non-invasive, non-electrical contact and low noise manner are necessary.

4. Conclusion

This research demonstrated the tunability of the front focal length of a fluidic lens by imposing CsWO$_3$ NPs' photothermal effect upon the lens frame made of the thermo-responsive PDMS, and was successfully implemented in a light sheet fluorescence microscope.

Empirically, the optical and photothermal properties of CsWO$_3$ NPs were examined, and the CsWO$_3$ NP solution-filled PDMS lens was designed, manufactured, characterized and implemented in the detection arm of LSFM for acquiring fluorescence images of green fluorescent μpowder and the fluorescein-coated CsWO$_3$ NPs. Experimental results confirmed that the PDMS fluidic lens is capable of photothermally tuning the front focal length for a range of 0.2 mm. In addition, the tuning of the working distance of the fluidic lens-incorporated detection arm in the LSFM successfully elucidated individual NPs with an enhancement of 1.47-fold in contrast ratio. Lastly, this research work demonstrated the feasibility of using the NIR-irradiated CsWO$_3$ NP solution as a heat source to modulate the thermo-optic and thermo-expansion effects of PDMS, enabling the tunability of the lens' focal length for fluorescence imaging, which is applicable to other optical systems that desire a delicate tuning of the focal plane without any electrical wiring.

Conflicts of interest

The authors declare no known competing or financial interests or personal relationships that could have appeared to influence the work reported in this paper.

Data availability

Data of the brightfield images for analyzing thermo-expansion effect, working distance of the converging objective lens, analysis of the lens' durability and repeatability, comparative table of actuation schemes, and photothermal and optical properties of the lens presented in the manuscript have been included as part of the SI. See DOI: https://doi.org/10.1039/d5ma00435g

Acknowledgements

This research work is financially supported by the National Science and Technology Council of Taiwan under grant# NSTC 112-2221-E-A49-022-MY3.

References

1 K. Machida and K. Adachi, Ensemble inhomogeneity of dielectric functions in Cs-doped tungsten oxide nanoparticles, *J. Phys. Chem. C*, 2016, **120**, 16919–16930.
2 J. Burgos, R. Mondragon, E. B. Elcioglu, F. Fabregat-Santiago and L. Hernandez, Experimental characterization and statistical analysis of water-based gold nanofluids for solar applications: optical properties and photothermal conversion efficiency, *Sol. RRL*, 2022, **6**, 2200104.
3 Q. Yang, C. Qin, N. Chen, H. Liu, B. Zhang and X. Wu, ZrC-Au core-shell nanoparticles for efficient solar photothermal conversion, *Int. J. Therm. Sci.*, 2024, **204**, 109175.
4 G. Palermo, U. Cataldl, L. Sio, T. Burgi, N. Tabiryan and C. Umeton, Optical control of plasmonic heating effects using reversible photo-alignment of nematic liquid crystals, *App. Phys. Lett.*, 2016, **109**, 191906.
5 G. Palermo, A. Guglielmelli, L. Pezzi, U. Cataldi, L. Sio, R. Caputo, A. Luca, T. Burgi, N. Tabiryan and C. Umeton, A command layer for anisotropic plasmonic photo-thermal effects in liquid crystal, *Liquid Cryst.*, 2018, **45**(13–15), 2214–2220.
6 G. Chen, Y. Lou, J. Li, L. Chen, Z. Xing, T. Zhang, D. Gu, Y. Peng and H. Wu, Transparent, self-healing, and defogging wearable devices enabled by plasmonic silver nanoparticle-embedded covalent-organic framework nanosheets, *ACS Mater. Lett.*, 2024, **6**, 648–655.
7 Y. Liu, L. Shi, X. Xu, P. Zhao, Z. Wang, S. Pu and X. Zhang, All-optical tuning of a magnetic-fluid-filled optofluidic ring resonator, *Lab Chip*, 2014, **14**, 3004.
8 P. Zhao, L. Shi, Y. Liu, Z. Wang, S. Pu and X. Zhang, Iron-oxide nanoparticles embedded silica microsphere resonator exhibiting broadband all-optical wavelength tunability, *Opt. Lett.*, 2014, **39**(13), 3845–3848.
9 A. Heber, M. Selmke and F. Cichos, Metal nanoparticle based all-optical photothermal light modulator, *ACS Nano*, 2014, **8**(2), 1893–1898.
10 M. A. Hernandez-Acosta, L. Soto-Ruvalcaba, C. L. Martinez-Gonzalez, M. Trejo-Valdez and C. Torres-Torres, Optical phase-change in plasmonic nanoparticles by a two-wave mixing, *Phys. Scr.*, 2019, **94**, 125802.
11 J. S. Donner, J. Morales-Dalmau, I. Alda, R. Marty and R. Quidant, Fast and transparent adaptive lens based on plasmonic heating, *ACS Photonics*, 2015, **2**, 355–360.
12 Y. Q. He, S. P. Liu, L. Kong and Z. F. Liu, A study on the sizes and concentrations of gold nanoparticles by spectra of absorption, resonance Rayleigh scattering and resonance non-linear scattering, *Spectrochim. Acta Part A*, 2005, **61**, 2861–2866.
13 A. Bahadur, A. Saeed, M. Shoaib, S. Iqbal, M. I. Bashir, M. Waqas, M. N. Hussain and N. Abbas, Eco-friendly synthesis of magnetite (Fe_3O_4) nanoparticles with tunable size: dielectric, magnetic, thermal and optical studies, *Mater. Chem. Phys.*, 2017, **198**, 229–235.
14 T. T. V. Phan, S. Mondal, M. Santhamoorthy, T. T. Truong, T. P. Nguyen and J. Oh, Hyaluronic acid functionalized iron-platinum nanoparticles for photothermal therapy and photoacoustic imaging, *Colloids Surf., B*, 2014, **238**, 113910.
15 Z. M. Markovic, L. M. Harhaji-Trajkovic, B. M. Todorovic-Markovic, D. P. Kepic, K. M. Arsikin, S. P. Jovanovic, A. C. Pantovic, M. D. Dramicanin and V. S. Trajkovic, In vitro comparison of the photothermal anticancer activity of graphene nanoparticles and carbon nanotubes, *Biomaterials*, 2011, **32**, 1121–1129.
16 B. Ji, H. Cai, Y. Yang, F. Peng, M. Song, K. Sun and F. Yan, Hybrid membrane camouflaged copper sulfide nanoparticles for photothermal-chemotherapy of hepatocellular carcinoma, *Acta Biomaterial*, 2020, **111**, 363–372.
17 C. Guo, S. Yin, H. Yu, S. Liu, Q. Dong, T. Goto, Z. Zhang, Y. Li and T. Sato, Photothermal ablation cancer therapy using homogeneous Cs_xWO_3 nanorods with broad near-infrared-red absorption, *Nanoscale*, 2013, **5**, 6469–6478.
18 A. Mata, A.J. Fleischman and S. Roy, Characterization of polydimethylsiloxane (PDMS) properties for biomedical micro/nanosystem, *Biomed. Microdevices*, 2005, **7**, 281–293.
19 E. Hecht, *Optics*, Addison Wesley, 4th edn, 2002.
20 Z. Zhu, L. Liu, Z. Liu, Y. Zhang and Y. Zhang, Surface-plasmon-resonance-based optical-fiber temperature sensor with high sensitivity and high figure of merit, *Opt. Lett.*, 2017, **42**(15), 2948–2951.